

Inclusion of the sample-tip interaction term in the theory of tip-enhanced Raman spectroscopy

Bruno C. Publico ¹, Bruno S. Oliveira,² Cassiano Rabelo ³, Hudson Miranda ³, Thiago L. Vasconcelos ²,
Ado Jorio ¹ and Luiz Gustavo Cançado ^{1,*}

¹*Departamento de Física, Universidade Federal de Minas Gerais, Belo Horizonte, Minas Gerais 30123-970, Brazil*

²*Divisão de Metrologia de Materiais, Instituto Nacional de Metrologia, Qualidade e Tecnologia, Duque de Caxias, Rio de Janeiro 25250-020, Brazil*

³*FabNS, Parque Tecnológico de Belo Horizonte - BHTec, Belo Horizonte, Minas Gerais 31.310-260, Brazil*



(Received 21 December 2021; revised 25 April 2022; accepted 19 May 2022; published 9 June 2022)

The scattering process in tip-enhanced Raman spectroscopy (TERS) can occur in distinct ways, depending on the number of interaction events and their respective time sequences. These events are fundamentally described by the interaction of the radiation field with the plasmonic nano-structure that generates local enhancement or with the scattering medium itself. The interactions are historically denominated as T, in reference to field-tip interaction, and S, referencing field-sample interaction. The TERS intensity was analytically derived for the ST and TST terms in *Phys. Rev. X* **4**, 031054 (2014). Here we provide further development on the TERS theory by presenting a comprehensive description of the physical picture and the mathematical steps for the obtention of analytical expressions that account for the TERS intensity related to the TS term for one- and two-dimensional samples. Finally, we performed a tip-approach TERS experiment in graphene with considerably higher accuracy than what has been reported in the literature and, with the inclusion of the TS term, the phonon coherence length of graphene, as measured by TERS, is revised to ≈ 40 nm.

DOI: [10.1103/PhysRevB.105.235414](https://doi.org/10.1103/PhysRevB.105.235414)

I. INTRODUCTION

The intensity in tip-enhanced Raman spectroscopy (TERS) experiments relies on the interaction between a plasmonic nanostructure and the scattering medium (sample) [1–8]. During the measurement, these two entities are kept at a relative distance short enough to allow radiation-matter interactions in the near-field regime [9]. In the most common case, the plasmonic nanostructure consists of a sharp metal tip coupled to a scanning probe microscopy (SPM) feedback system that controls the tip-sample distance [8,10–12]. Greater local enhancement is achieved if the tip supports local surface plasmon resonance (LSPR) at the wavelength specified by the excitation or scattered field [13–15]. This is the case of the recently developed plasmon-tunable tip pyramids (PTTPs), which have demonstrated great performance in terms of field enhancement with excellent reproducibility rate [16,17].

The scattering process in TERS can occur in distinct ways, depending on the number of interaction events and their respective time sequences [18,19]. These events are fundamentally described by the interaction of the radiation field with the plasmonic nanostructure or the scattering medium. The interactions are historically denominated as T, in reference to field-tip interaction, and S, referencing field-sample interaction [18]. The simpler cases are illustrated in Figs. 1(a) and 1(b). In Fig. 1(a), the incident field with frequency ω_0 interacts with the tip and the secondary field generated by the

tip (also with frequency ω_0) reaches the sample. Afterwards, the Raman-scattered field with frequency ω_s goes directly to the detector. This sequence is denominated ST, which reads *tip sample*. Notice that an operator notation is used and, as such, the time sequence reads backwards [18]. Figure 1(b) illustrates the opposite sequence: the incident field first reaches the sample and the Raman-scattered field interacts with the tip. In this case, the field that reaches the detector is the secondary scattered component, generated by the tip, with frequency ω_s . This sequence is denominated TS, which reads *sample tip*. The next higher-order sequence is the *tip-sample-tip* sequence, represented as TST and illustrated in Fig. 1(c). In TST, the incident field reaches the tip and the secondary field with frequency ω_0 generated by the tip excites the sample. The Raman process takes place and the scattered field with frequency ω_s interacts with the tip. Finally, the tip generates another secondary field with frequency ω_s that propagates towards the detector.

Each interaction with the tip provides a local enhancement of the radiation field. The level of enhancement depends on the plasmonic properties of the tip and is quantified by the field-enhancement factor f_e . Since the local field interacts once with the nanoplasmonic structure (tip) in the ST and TS cases and twice in the TST case, the intensity of the Raman scattered field measured at the detector accounts for two terms proportional to f_e^2 , derived from ST and TS sequences, and for one term proportional to f_e^4 , derived by the TST sequence [20,21]. As f_e increases, the TST sequence becomes more dominant, unless destructive interference effects take place, as discussed below. Higher-order terms may also occur, but the lower associated probability reduces their importance [18].

*cancado@fisica.ufmg.br

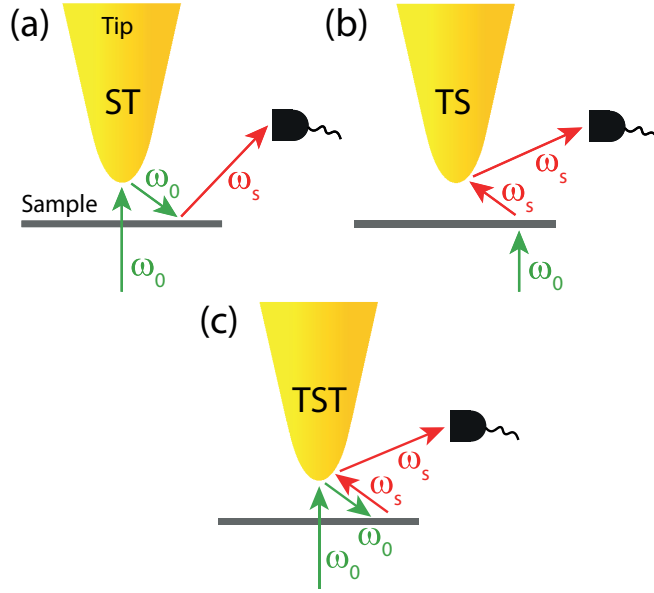


FIG. 1. Scattering processes in TERS. (a) *Tip sample* (ST). The incident field with frequency ω_0 interacts with the tip and the secondary field generated by the tip (also with frequency ω_0) reaches the sample. Afterwards, the Raman-scattered field with frequency ω_s goes directly to the detector. (b) *Sample tip* (TS). The incident field first reaches the sample and the Raman-scattered field interacts with the tip. In this case, the field that reaches the detector is the secondary scattered component with frequency ω_s generated by the tip. (c) *Tip sample tip* (TST). The incident field reaches the tip and the secondary field with frequency ω_0 generated by the tip excites the sample. The Raman process takes place and the Raman field with frequency ω_s interacts with the tip. Finally, the tip generates another secondary field with frequency ω_s which propagates towards the detector.

Another aspect to be taken into account in the description of the TERS intensity is the degree of coherence of the radiation field in the near-field regime. Given that the minimal coherence length of the optical field is not limited to $\lambda/2$ in the near-field regime [22], as it is in the far field [23], scattering components derived from different regions of the sample's surface can interfere at the plasmonic nanostructure in TERS [19,20,24–26]. Interference is especially important for the TS and TST terms, in which the Raman field emitted by the sample interacts with the tip before propagating to the detector [19,20]. Due to the symmetry of the polarizability-derivative tensor and consequently to the polarization geometry of the Raman-scattered field, the interference is constructive for fields generated by totally symmetric vibrational modes and destructive otherwise [27]. This difference has allowed the determination of the phonon coherence length in graphene [26,28] and GaAs [29].

Detailed analytical calculations of the TST and ST terms were presented in Ref. [19] and applied in Ref. [26] for the interpretation of TERS measurements of graphene. Later on, the TS term was included in the analysis of TERS data measured in graphene nanoflakes [20] and GaAs [29]. However, the analytical calculations for the TS term have never been reported. The aim of this paper is to provide a further development on the TERS theory by presenting a comprehensive

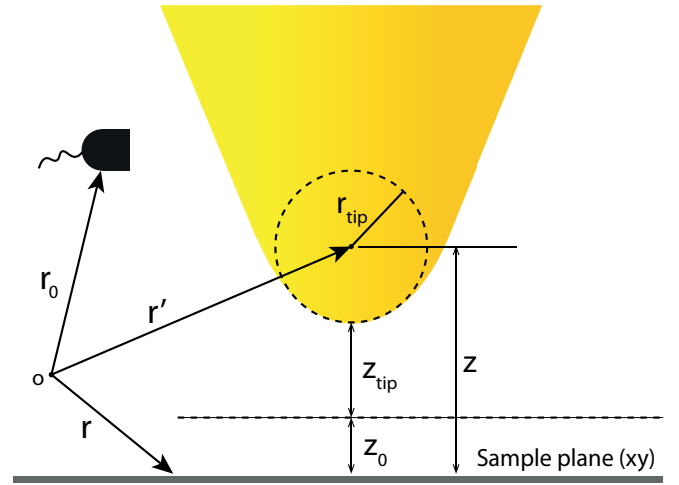


FIG. 2. Geometrical parameters in our TERS model. The sample lies on the xy plane and the tip (gold colored) is aligned with the z direction. The field generated by the tip is described by the field of a point dipole aligned with the z direction and positioned at $\mathbf{r}' = (0, 0, z)$. r_{tip} is the radius of the tip's apex and the spatial coordinate at the sample plane is described by $\mathbf{r} = (x, y, 0)$. The detector is located at \mathbf{r}_0 . z_{tip} is the distance between the apex of the tip and the minimal separation z_0 between the tip and the sample plane, as defined by the AFM sensitive feedback system.

description of the physical picture and the mathematical steps for deriving analytical expressions that account for the TERS intensity related to the TS term in one- and two-dimensional (1D and 2D, respectively) samples. This work fulfills a gap of information in the literature, complementing the analysis of TERS intensity presented in a series of Physical Review papers dedicated to the subject [19,20,24–27,30].

II. CALCULATION OF THE TS INTERACTION IN 2D SYSTEMS

The general picture of the TERS intensity was already presented in Ref. [19] and will be briefly summarized here for minimal self-consistency. The physical system is schematically illustrated in Fig. 2. It is composed by the sample lying on the xy plane and by the tip whose shaft is aligned along the z direction. The field generated by the tip is described as the field of a point-dipole aligned with the z direction and positioned at $\mathbf{r}' = (0, 0, z)$. In this case, the zz component is the only non-null term of the tip's polarizability tensor and is given by $\alpha_{||}(\omega) = 2\pi r_{\text{tip}}^3 f_e(\omega)$, with ω being the angular frequency of the radiation field under consideration and r_{tip} the radius of the tip's apex, as illustrated in Fig. 2. The spatial coordinate at the sample plane is described by $\mathbf{r} = (x, y, 0)$.

The intensity of the TERS field with frequency ω_s measured at the detector located at \mathbf{r}_0 is evaluated by considering the ensemble average of the scattered field on the form [19]

$$\begin{aligned}
 S(\mathbf{r}_0, \omega_s) = & \frac{\omega_s^4}{\epsilon_0^2 c^4} \iint_{\mathbb{D}} \langle \alpha^{\gamma*}(\mathbf{r}_1; \omega_s, \omega_0) \alpha^{\gamma}(\mathbf{r}_2; \omega_s, \omega_0) \rangle \\
 & \times [\mathbf{G}(\mathbf{r}_0, \mathbf{r}_1) \mathbf{E}(\mathbf{r}_1, \omega_0)]^* \mathbf{G}(\mathbf{r}_0, \mathbf{r}_2) \\
 & \times \mathbf{E}(\mathbf{r}_2, \omega_0) d^3 \mathbf{r}_1 d^3 \mathbf{r}_2,
 \end{aligned} \quad (1)$$

where ε_0 and c are the free-space permittivity and speed of light, respectively, \mathbf{G} is the dyadic Green's function tensor, $\mathbf{E}(\omega_0)$ is the excitation vector field with frequency ω_0 , and the term between brackets accounts for the spatial correlation between the Raman tensor component α^γ related to a vibrational mode γ with frequency ω_s , evaluated at the positions \mathbf{r}_1 and \mathbf{r}_2 at the sample plane. This correlation function is assumed to have a Gaussian profile whose width is considered to be the coherence length L_c of the phonon mode γ under consideration. The integrals run over the sample domain \mathbb{D} . In the limit $\mathbb{D} \gg z$, a more explicit form of Eq. (1) can be written as

$$\begin{aligned} S(\mathbf{r}_0, \omega_s) &= \frac{\omega_s^4}{\varepsilon_0^2 c^4} \sum_{l,m,n} \sum_{i,j} \iint_{-\infty}^{+\infty} dx_2 dy_2 G_{ln}(\mathbf{r}_0, x_2, y_2; \omega_s) \\ &\times \alpha_{nj}^\gamma(x_2, y_2; \omega_s, \omega_0) E_j(x_2, y_2; \omega_0) \\ &\times \iint_{-\infty}^{+\infty} dx_1 dy_1 \left[\frac{e^{-[(x_1-x_2)^2+(y_1-y_2)^2]/L_c^2}}{\pi L_c^2} \right] \\ &\times G_{lm}^*(\mathbf{r}_0, x_1, y_1; \omega_s) \alpha_{mi}^{\gamma*}(x_1, y_1; \omega_s, \omega_0) \\ &\times E_i^*(x_1, y_1; \omega_0), \end{aligned} \quad (2)$$

where $l \in \{x, y, z\}$ and $m, n, i, j \in \{x, y\}$. Performing the steps explained in Ref. [19], the fourfold integral in Eq. (2) can be replaced by the following twofold integral in the spatial frequency domain

$$\begin{aligned} S(\mathbf{r}_0, \omega_s) &= 4\pi^2 \frac{\omega_s^4}{\varepsilon_0^2 c^4} \sum_{l,m,n} \sum_{i,j} \alpha_{mi}^{\gamma*} \alpha_{nj}^\gamma \iint_{-\infty}^{+\infty} \\ &\times dk_x dk_y \hat{F}_{lm}^*(k_x, k_y) \hat{F}_{lnj}(k_x, k_y) e^{-(k_x^2+k_y^2)L_c^2/4}, \end{aligned} \quad (3)$$

with $\hat{F}_{lnj}(k_x, k_y)$ defined as the Fourier transform of the product $G_{ln}(\mathbf{r}_0, x_2, y_2)E_j(x_2, y_2; \omega_0)$ on the form

$$\begin{aligned} \hat{F}_{lnj}(k_x, k_y) &= \frac{1}{4\pi^2} \iint_{-\infty}^{+\infty} dx_2 dy_2 G_{ln}(\mathbf{r}_0, x_2, y_2) \\ &\times E_j(x_2, y_2; \omega_0) e^{-i(k_x x_2 + k_y y_2)}. \end{aligned} \quad (4)$$

Similarly, $\hat{F}_{lmi}(k_x, k_y)$ is defined as the Fourier transform of the product $G_{lm}(\mathbf{r}_0, x_1, y_1)E_i(x_1, y_1; \omega_0)$.

TS processes start with the incident field interacting with the sample. The Raman-scattered field then interacts with the tip at $\mathbf{r}' = (0, 0, z)$, prior to become the propagating field that reaches the detector at \mathbf{r}_0 . In this case, the $G_{ln}\alpha_{nj}^\gamma E_j$ product assumes the form [19]

$$\begin{aligned} G_{ln}(\mathbf{r}_0, x, y; \omega_s) \alpha_{nj}^\gamma(x, y; \omega_s, \omega_0) E_j(x, y, \omega_0) \\ = \frac{\omega_s^2}{\varepsilon_0 c^2} G_{lz}^o(\mathbf{r}_0, z; \omega_s) \alpha_{||}(\omega_s) G_{zn}^o(z, x, y; \omega_s) \\ \times \alpha_{nj}^\gamma(x, y; \omega_s, \omega_0) E_j(x, y, \omega_0) \end{aligned} \quad (5)$$

and Eq. (4) becomes

$$\begin{aligned} \hat{F}_{lnj}(k_x, k_y) &= \frac{1}{4\pi^2} \frac{\omega_s^2}{\varepsilon_0 c^2} G_{lz}^o(\mathbf{r}_0, z; \omega_s) \alpha_{||}(\omega_s) \\ &\times \iint_{-\infty}^{+\infty} dx_2 dy_2 G_{zn}^o(z, x_2, y_2; \omega_s) \\ &\times E_{0j}(x_2, y_2; \omega_0) e^{-i(k_x x_2 + k_y y_2)}. \end{aligned} \quad (6)$$

Considering only the near-field term of the dyadic Green's function, the $G_{zn}^o(z, x, y; \omega_s)$ component is

$$G_{zn}^o(z, x, y; \omega_s) = \frac{c^2}{4\pi \omega_s^2} \frac{3zn}{(x^2 + y^2 + z^2)^{5/2}}. \quad (7)$$

Substitution of (7) in (6) gives

$$\begin{aligned} \hat{F}_{lnj}(k_x, k_y) &= \frac{3}{16\pi^3} \frac{z}{\varepsilon_0} G_{lz}^o(\mathbf{r}_0, z; \omega_s) \alpha_{||}(\omega_s) \\ &\times \iint_{-\infty}^{+\infty} dx_2 dy_2 \frac{n}{(x_2^2 + y_2^2 + z^2)^{5/2}} \\ &\times E_{0j}(x_2, y_2, \omega_0) e^{-i(k_x x_2 + k_y y_2)}. \end{aligned} \quad (8)$$

Because in TS the incident field interacts with the sample first, it is important to determine the polarization of the incident field. Here we consider a radially polarized beam, which has a strong component along the z direction at the focal plane. This out-of-plane component is important to maximize the interaction of the incident field with the tip in the ST and TST processes [19,27,30,31]. For an objective lens with NA = 1.4, the amplitude of the in-plane component of the radially polarized incident field is approximately three times smaller than the out-of-plane component at the focal plane [9]. Therefore, by considering the amplitude of the out-of-plane component as E_0 (to be consistent with the notation used in Ref. [19]), the incident field assumes the approximate form in the focal xy plane

$$\mathbf{E}(\omega_0) = \frac{E_0(\omega_0)}{\sqrt{3}} \begin{bmatrix} \cos(\phi) \\ \sin(\phi) \\ \sqrt{3} \end{bmatrix}, \quad (9)$$

where ϕ is the polarization angle on the xy plane, measured from the x axis. From Eq. (9), we have $E_{0j}(x, y; \omega_0) = E_0(\omega_0) j / [\sqrt{3}(x^2 + y^2)^{1/2}]$. Substitution in Eq. (8) leads to

$$\begin{aligned} \hat{F}_{lnj}(k_x, k_y) &= \frac{\sqrt{3}z}{16\pi^3 \varepsilon_0} G_{lz}^o(\mathbf{r}_0, z; \omega_s) \alpha_{||}(\omega_s) E_0(\omega_0) \\ &\times \iint_{-\infty}^{+\infty} dx_2 dy_2 \frac{n j e^{-i(k_x x_2 + k_y y_2)}}{(x_2^2 + y_2^2 + z^2)^{5/2} (x_2^2 + y_2^2)^{1/2}}. \end{aligned} \quad (10)$$

Substitution of the Fourier component (10) in Eq. (3) (similarly for \hat{F}_{lmi}) allows the analytical evaluation of the contribution of the TS term to the TERS intensity. As an example, we perform this calculation for the two main Raman features of graphene, namely the first-order bond-stretching

G band, at $\approx 1580 \text{ cm}^{-1}$, and the two-phonon G' band (also called 2D band in the literature), at $\approx 2700 \text{ cm}^{-1}$. While the G band is a twofold degenerated zone-center phonon with E_{2g} symmetry, the G' band belongs majorally to a totally symmetric transversal optical phonon branch near the corner of the first Brillouin zone (K or K' point) [27,32]. The Raman tensors for these optical phonons are [33]

$$\begin{aligned} \tilde{\alpha}^G(E_{2g1}) &= \alpha^{E_{2g}} \begin{bmatrix} 1 & 0 \\ 0 & -1 \end{bmatrix}, & \tilde{\alpha}^G(E_{2g2}) &= \alpha^{E_{2g}} \begin{bmatrix} 0 & 1 \\ 1 & 0 \end{bmatrix}, \\ \tilde{\alpha}^{G'}(A_1) &= \alpha^{A_1} \begin{bmatrix} 1 & 0 \\ 0 & 1 \end{bmatrix}, \end{aligned} \quad (11)$$

where E_{2g1} and E_{2g2} are the two modes that compose the double-degenerated G band. The out-of-plane components are omitted in (11), because they are null for the E_{2g} modes and negligible for the A_1 mode [30].

For the Raman modes listed in Eq. (11), we have $n, j \in \{x, y\}$ in Eq. (10). This integral has a complicated analytical form. Following the same procedure as in Ref. [19], developed for the ST and TST sequences, we approximate the integrand of Eq. (10) of a linear combination of Gaussian peaks on the form

$$\begin{aligned} & \frac{nj}{(x^2 + y^2 + z^2)^{5/2}(x^2 + y^2)^{1/2}} \\ & \approx \frac{nj}{z^6} [a_0 e^{-b_0(x^2+y^2)/z^2} + c_0 e^{-d_0(x^2+y^2)/z^2} + e_0 e^{-f_0(x^2+y^2)/z^2} \\ & + g_0 e^{-h_0(x^2+y^2)/z^2} + p_0 e^{-q_0(x^2+y^2)/z^2}], \end{aligned} \quad (12)$$

where $\{a_0, b_0, c_0, d_0, e_0, f_0, g_0, h_0, p_0, q_0\}$ are numerical parameters to be determined. A least-square fit of the original function with (12) revealed $a_0 = 13.57$, $b_0 = 110.81$, $c_0 = 4.1$, $d_0 = 16.61$, $e_0 = 1.99$, $f_0 = 4.08$, $g_0 = 0.48$, $h_0 = 1.30$, $p_0 = 0.02$, and $q_0 = 0.33$. Next, we take the Fourier transform of Eq. (12) as

$$\begin{aligned} \hat{h}_{nj}(k_x, k_y; z) &= \iint_{-\infty}^{+\infty} dx dy (nj) e^{-i(k_x x + k_y y)} \\ & \times [a_0 e^{-b_0(x^2+y^2)/z^2} + c_0 e^{-d_0(x^2+y^2)/z^2} \\ & + e_0 e^{-f_0(x^2+y^2)/z^2} + g_0 e^{-h_0(x^2+y^2)/z^2} \\ & + p_0 e^{-q_0(x^2+y^2)/z^2}]. \end{aligned} \quad (13)$$

This integral can be readily solved analytically. Next, Eq. (10) is rewritten in terms of the Fourier component $\hat{h}_{nj}(k_x, k_y; z)$ evaluated in (13) and assumes the form

$$\hat{F}_{lnj}(k_x, k_y) = \frac{\sqrt{3}}{16\pi^3} \frac{E_0(\omega_0)}{\varepsilon_0 z^5} G_{l_z}^o(\mathbf{r}_0, z; \omega_s) \alpha_{\parallel}(\omega_s) \hat{h}_{nj}(k_x, k_y; z). \quad (14)$$

Analogously,

$$\begin{aligned} \hat{F}_{lmi}^*(k_x, k_y) &= \frac{\sqrt{3}}{16\pi^3} \frac{E_0^*(\omega_0)}{\varepsilon_0 z^5} \\ & \times G_{l_z}^{o*}(\mathbf{r}_0, z; \omega_s) \alpha_{\parallel}^*(\omega_s) \hat{h}_{mi}^*(k_x, k_y; z). \end{aligned} \quad (15)$$

Substitution of Eqs. (14) and (15) in Eq. (3) yields

$$\begin{aligned} S^{\text{TS}}(\mathbf{r}_0) &= \frac{3\omega_s^4}{64\pi^4 \varepsilon_0^4 c^4 z^{10}} \sum_l |\alpha_{\parallel}(\omega_s) G_{l_z}^o(\mathbf{r}_0, z; \omega_s) E_0(\omega_0)|^2 \\ & \times \left[\sum_{m,n} \sum_{i,j} \tilde{\alpha}_{mi}^{\gamma*}(\omega_s) \tilde{\alpha}_{nj}^{\gamma}(\omega_s) \iint_{-\infty}^{+\infty} \right. \\ & \times dk_x dk_y \hat{h}_{mi}^*(k_x, k_y; z) \hat{h}_{nj}(k_x, k_y; z) e^{-(k_x^2 + k_y^2)L_c^2/4} \left. \right]. \end{aligned} \quad (16)$$

Defining the function

$$\begin{aligned} \Psi_{mi,nj}(z; L_c) &= \iint_{-\infty}^{+\infty} dk_x dk_y \hat{h}_{mi}^*(k_x, k_y; z) \\ & \times \hat{h}_{nj}(k_x, k_y; z) e^{-(k_x^2 + k_y^2)L_c^2/4}, \end{aligned} \quad (17)$$

Eq. (16) can be written in the compact form

$$\begin{aligned} S^{\text{TS}}(\mathbf{r}_0) &= \frac{3\omega_s^4}{64\pi^4 \varepsilon_0^4 c^4 z^{10}} \sum_l |\alpha_{\parallel}(\omega_s) G_{l_z}^o(\mathbf{r}_0, z; \omega_s) E_0(\omega_0)|^2 \\ & \times \sum_{m,n} \sum_{i,j} \tilde{\alpha}_{mi}^{\gamma*}(\omega_s, \omega_0) \tilde{\alpha}_{nj}^{\gamma}(\omega_s, \omega_0) \Psi_{mi,nj}(z; L_c). \end{aligned} \quad (18)$$

In the following, we insert in Eq. (18) the values of the components of the Raman polarizability tensor associated with the phonon mode γ , $\tilde{\alpha}_{mi}^{\gamma*}$ and $\tilde{\alpha}_{nj}^{\gamma}$, as given in Eq. (11). We also notice that $\alpha_{\parallel}(\omega_s) = 2\pi \varepsilon_0 r_{\text{tip}}^3 f_e(\omega_s)$ [9], recalling that f_e is the field enhancement factor and r_{tip} is the radius of the apex of the near-field probe (see Fig. 2). With these considerations, for the G' mode, the signal is finally given as

$$\begin{aligned} S_G^{\text{TS}}(\mathbf{r}_0) &= \frac{3\omega_s^4 r_{\text{tip}}^6 \tilde{f}_e^2(\omega)}{8\pi^2 \varepsilon_0^2 c^4 z^{10}} \sum_l |G_{l_z}^o(\mathbf{r}_0, z; \omega_s)|^2 \\ & \times \tilde{\alpha}^{A_1}(\omega_s, \omega_0) E_0(\omega_0)^2 \\ & \times [\Psi_{xx,xx}(z; L_c) + \Psi_{xx,yy}(z; L_c)], \end{aligned} \quad (19)$$

with $\tilde{f}_e = \text{Re}[f_e]$. For the G mode, the sum of the signals of the E_{2g1} and E_{2g2} components leads to

$$\begin{aligned} S_G^{\text{TS}}(\mathbf{r}_0) &= \frac{3\omega_s^4 r_{\text{tip}}^6 \tilde{f}_e^2(\omega)}{8\pi^2 \varepsilon_0^2 c^4 z^{10}} \sum_l |G_{l_z}^o(\mathbf{r}_0, z; \omega_s)|^2 \\ & \times \tilde{\alpha}^{E_{2g}}(\omega_s, \omega_0) E_0(\omega_0)^2 \\ & \times [\Psi_{xx,xx}(z; L_c) - \Psi_{xx,yy}(z; L_c) + 2\Psi_{xy,yx}(z; L_c)]. \end{aligned} \quad (20)$$

Figures 3(a) and 3(b) show the plot of the TS signal (red curve) for the A_1 and E_{2g} modes, respectively, as a function of z_{tip} , the distance between the apex of the tip and the minimal separation z_0 between the tip and the sample plane, as defined by the feedback system. As illustrated in Fig. 2, $z_{\text{tip}} = z - (r_{\text{tip}} + z_0)$, noting that z is the vertical position, measured from the sample plane, of the point dipole considered as the source of the secondary field generated by the plasmonic structure. For this specific example, we chose $r_{\text{tip}} = 15 \text{ nm}$, $L_c = 50 \text{ nm}$, $f_e = 6$, and $z_0 = 5 \text{ nm}$. Blue and black curves represent the TST and ST signals, respectively, as

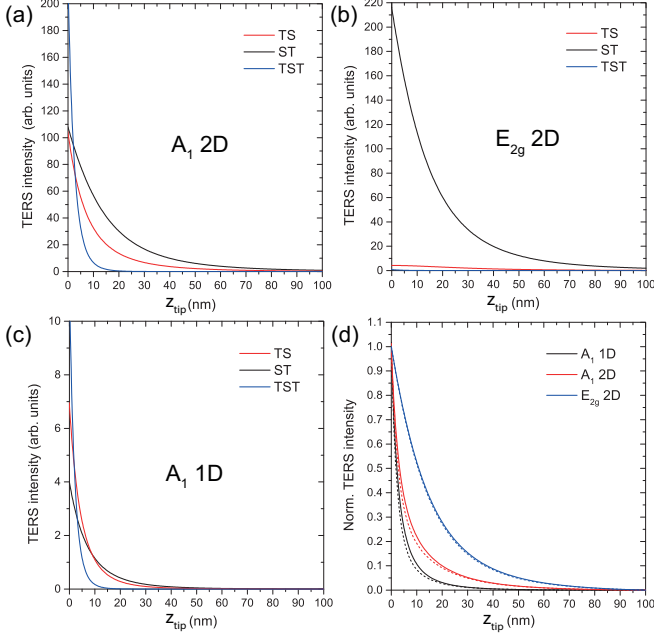


FIG. 3. (a), (b) Plots of the TS signal (red curve) for the A_1 and E_{2g} modes, respectively, as a function of $z_{\text{tip}} = z - (r_{\text{tip}} + z_0)$ (as illustrated in Fig. 2). For this specific example, we chose $r_{\text{tip}} = 15$ nm, $L_c = 50$ nm, $f_e = 6$, and $z_0 = 5$ nm. Blue and black curves represent the TST and ST signals, respectively, as a function of z_{tip} , based on the results derived in Ref. [19]. For the A_1 mode, panel (a), the z dependence of the TST mode is steeper than for the ST and TS events which, in turn, have approximately the same importance at $z_{\text{tip}} = 0$. As shown in panel (b), the TERS signal for the E_{2g} mode at z_0 is completely dominated by the ST term, because the Raman field undergoes destructive interference at the tip in the TST and TS processes [19,20,26]. (c) Plot of the TS signal (red curve) for the A_1 mode in a one-dimensional system as a function of z_{tip} , according to Eq. (29). The plots for the TST and ST signals are shown (blue and black curves, respectively), as evaluated in Ref. [19]. As for the A_1 mode in two-dimensional systems, the TST component is steeper and dominates at the minimal tip-sample distance, $z_{\text{tip}} = 0$. The visual comparison of panels (a) and (c) clearly shows that the z dependence is steeper for the TERS signal in 1D systems than in 2D systems, as discussed in Ref. [25]. (d) Plot of the normalized sum of the TST, TS, and ST signals (solid lines) as a function of z_{tip} for the A_1 mode in 1D and 2D systems (black and red solid curves, respectively) and also for the E_{2g} mode in 2D systems (blue solid curve). The dashed lines are the same plots, but considering only the TST and ST signals, as in Ref. [19].

a function of z_{tip} . The TST and ST signals were calculated in Ref. [19] and are reproduced here for comparison. As shown in Fig. 3(a), for the A_1 mode, which gives rise to the G' band in graphene, the z dependence of the TST sequence is steeper than the ST and TS, being considerably stronger at $z_{\text{tip}} = 0$. This is expected, since both incident and scattered fields are enhanced by the tip in the TST process. The ST and TS signals have approximately the same importance at $z_{\text{tip}} = 0$, as expected by symmetry. As shown in Fig. 3(b), the situation is drastically different for the E_{2g} mode, which gives rise to the G band in graphene. In this case, the TERS signal at $z_{\text{tip}} = 0$ is completely dominated by the ST term, since the Raman field

undergoes destructive interference at the tip in the TST and TS processes, as discussed in detail in Refs. [19,20,26].

III. CALCULATION OF THE TS INTERACTION IN 1D SYSTEMS

Optical absorption in 1D systems is highly anisotropic, being strong for light polarized along their elongation and practically null for light polarized along the transversal direction. By taking into account this depolarization effect for an object aligned along the x direction, Eq. (3) can be adapted to the 1D case, assuming the form [19]

$$S(\mathbf{r}_0, \omega_s) = 2\pi \frac{\omega_s^4}{\varepsilon_0^2 c^4} \sum_l \tilde{\alpha}_{xx}^{\gamma*} \tilde{\alpha}_{xx}^{\gamma} \int_{-\infty}^{+\infty} \times dk_x \hat{F}_{lx}^*(k_x) \hat{F}_{lx}(k_x) e^{-(k_x^2 L_c^2)/4}. \quad (21)$$

For the TS term, the reverse Fourier transform of $\hat{F}_{lx}(k_x)$ is given by

$$\hat{F}_{lx}(k_x) = \frac{1}{2\pi} \frac{\omega_s^2}{\varepsilon_0 c^2} \alpha_{\parallel}(\omega_s) G_{l_z}^{\circ}(\mathbf{r}_0, z; \omega_s) \int_{-\infty}^{+\infty} \times dx G_{zx}^{\circ}(x, z; \omega_s) E_{0x}(x, y; \omega_0) e^{-ik_x x}. \quad (22)$$

Considering only the near-field term, the dyadic Green's function $G_{zx}^{\circ}(x, z; \omega_s)$ assumes the approximate form

$$G_{zx}^{\circ}(x, z; \omega_s) = \frac{c^2}{4\pi \omega_s^2} \frac{3zx}{(\sqrt{x^2 + z^2})^5}. \quad (23)$$

Also, from Eq. (9), the x component of the incident field can be written in terms of the amplitude E_0 as $E_{0x} = E_0/\sqrt{3}$. With these considerations, Eq. (22) becomes

$$\hat{F}_{lx}(k_x) = \frac{\sqrt{3}z}{8\pi^2 \varepsilon_0} \alpha_{\parallel}(\omega_s) G_{l_z}^{\circ}(\mathbf{r}_0, z; \omega_s) E_0(\omega_0) \times \int_{-\infty}^{+\infty} dx \frac{x e^{-ik_x x}}{(\sqrt{x^2 + z^2})^5}. \quad (24)$$

By taking $y = 0$ and $n = j = x$, the approximation (12) applies to (24), which turns into

$$\hat{F}_{lx}(k_x) = \frac{\sqrt{3}}{8\pi^2 \varepsilon_0 z^5} \alpha_{\parallel}(\omega_s) G_{l_z}^{\circ}(\mathbf{r}_0, z; \omega_s) E_0(\omega_0) \times \int_{-\infty}^{+\infty} dx x^2 e^{-ik_x x} [a_0 e^{-b_0 x^2/z^2} + c_0 e^{-d_0 x^2/z^2} + e_0 e^{-f_0 x^2/z^2} + g_0 e^{-h_0 x^2/z^2} + p_0 e^{-q_0 x^2/z^2}]. \quad (25)$$

To shorten the notation, we define the functions $\hat{f}_x(k_x; z)$ and $\varphi_{xx}(z; L_c)$, respectively, as

$$\hat{f}_x(k_x; z) = \int_{-\infty}^{+\infty} dx [a_0 e^{-b_0 x^2/z^2} + c_0 e^{-d_0 x^2/z^2} + e_0 e^{-f_0 x^2/z^2} + g_0 e^{-h_0 x^2/z^2} + p_0 e^{-q_0 x^2/z^2}] x^2 e^{-ik_x x} \quad (26)$$

and

$$\varphi_{xx}(z; L_c) = \int_{-\infty}^{+\infty} dk_x \hat{f}_x(k_x; z) \hat{f}_x^*(k_x; z) e^{-(k_x^2 L_c^2)/4}. \quad (27)$$

Next, Eqs. (25), (26), and (27) can be used to rewrite the TS signal (21) as

$$S^{\text{TS}}(\mathbf{r}_0) = \frac{3\omega_s^4 r_{\text{tip}}^6 \tilde{f}_e^2(\omega)}{8\pi \varepsilon_0^2 c^4 z^{10}} \sum_l \tilde{\alpha}_{xx}^{\nu*}(\omega_s, \omega_0) \tilde{\alpha}_{xx}^{\nu}(\omega_s, \omega_0) \left| G_{l_z}^{\circ}(\mathbf{r}_0, z; \omega_s) E_0(\omega_0) \right|^2 \varphi_{xx}(z; L_c), \quad (28)$$

where we have considered $\alpha_{\parallel}(\omega) = 2\pi \varepsilon_0 r_{\text{tip}}^3 f_e(\omega)$.

A good example of a Raman mode derived from a 1D nanosystem is the disorder-induced D band ($\approx 1350 \text{ cm}^{-1}$) measured from a graphene edge [34]. The D band derives from the same totally symmetric phonon as the G' band [32]. For this mode, we simply have $\tilde{\alpha}_{xx}^{\nu*} \tilde{\alpha}_{xx}^{\nu} = |\tilde{\alpha}^{A_1}(\omega_s, \omega_0)|^2$ and the signal (28) assumes the form

$$S^{\text{TS}}(\mathbf{r}_0) = \frac{3\omega_s^4 r_{\text{tip}}^6 \tilde{f}_e^2(\omega)}{8\pi \varepsilon_0^2 c^4 z^{10}} \sum_l \left| G_{l_z}^{\circ}(\mathbf{r}_0, z; \omega_s) \tilde{\alpha}^{A_1} \right|^2 \varphi_{xx}(z; L_c). \quad (29)$$

Figure 3(c) shows the plot of the TS signal (red curve) for the A_1 mode in a one-dimensional system as a function of z_{tip} , according to Eq. (29). As for the two-dimensional case, we chose $r_{\text{tip}} = 15 \text{ nm}$, $L_c = 50 \text{ nm}$, $f_e = 6$, and $z_0 = 5 \text{ nm}$. The same plots for the TST and ST signals are shown (blue and black curves, respectively). The z dependences of the TST and ST signals were evaluated in Ref. [19]. As for the A_1 mode in two-dimensional systems, the TST component is steeper and dominates at the minimal tip-sample distance z_0 . The visual comparison between Figs. 3(a) and 3(c) clearly shows that the z dependence is steeper for the TERS signal from 1D systems than from 2D systems, as discussed in Ref. [25].

IV. APPLYING THE THEORY TO EXPERIMENTAL DATA

Figure 3(d) summarizes the results of Secs. II and III by showing the plot of the normalized sum of the TST, TS, and ST signals (solid lines) as a function of z_{tip} for the A_1 mode in 1D and 2D systems (black and red solid curves, respectively), and also for the E_{2g} mode in 2D systems (blue solid curve). As for the panels 3(a)–3(c), we have considered $r_{\text{tip}} = 15 \text{ nm}$, $L_c = 50 \text{ nm}$, $f_e = 6$, and $z_0 = 5 \text{ nm}$. The dashed lines are the same plots, but considering only the TST and ST signals, as in Ref. [19]. The comparison shows that, in general, the inclusion of the TS term turns the z dependence slightly less steeper.

To test the validity of the theory, we have performed the tip-approach TERS experiment in graphene, with a considerably higher degree of accuracy than what has been reported in the literature [26], and the results are presented in Fig. 4. The tip-enhanced Raman setup is based on an inverted optical microscope equipped with an x, y -scan stage. The sample is a mechanically exfoliated graphene deposited on the top of a 200- μm -thick cover glass serving as a dielectric transparent substrate. A high numerical aperture objective (1.4 NA) is used to focus a radially polarized laser beam with 632.8 nm of wavelength on the sample plane. The plasmonic probe is a plasmon-tunable tip pyramid (PTTP) [16,17] positioned at the center of the focus area. This PTTP has a nanopyramid with

lateral length of 470 nm, matching the resonance condition for the second LSPR monopole mode with the laser energy (1.96 eV) [16]. The PTTP is attached to a quartz tuning fork and kept at a distance of $\approx 5 \text{ nm}$ from the sample's surface by means of a shear-force feedback system. The scattered light is collected in backscattering geometry (through the same objective lens), filtered by a notch filter which suppresses the Rayleigh component of the scattered light. The Raman signal is then dispersed in a spectrograph and recorded by a cooled charge-coupled device (CCD). The tip-enhanced Raman image is obtained from hyperspectral analysis. More details on the setup can be found in Ref. [12].

Figures 4(a) and 4(b) show two components of a hyperspectral TERS map of a graphene edge, where the color scales render the G' and D intensities, respectively. While the G' band spreads over the whole graphene area, the D band is confined at the edge, which therefore behaves as a one-dimensional scatter [34]. Figure 4(c) shows a scanning electron microscopy (SEM) image of the PTTP used in the experiment. The yellow circle with diameter of 30 nm provides visual reference for $r_{\text{tip}} \approx 15 \text{ nm}$. Figure 4(d) shows TERS spectra recorded at the edge of the graphene flake, at the position indicated by the light-blue circle in Fig. 4(b), with the tip positioned at $z_{\text{tip}} = 0$ (black spectrum) and $z_{\text{tip}} = 30 \text{ nm}$ (red spectrum). All bands are enhanced as the tip approaches the sample plane but, due to its 1D character, the D band enhances considerably more. Besides, because the G band undergoes destructive interference and the G' band undergoes constructive interference in the TS and TST processes, the G band enhances less than the G' . The normalized TERS intensities are plotted in Fig. 4(d), as functions of z_{tip} . The graphic clearly shows the distinct behaviors of the D , G , and G' bands. The solid curves are theoretical curves fitted to the data, where the regression converged to $r_{\text{tip}} = 15 \text{ nm}$ (fixed, as revealed by SEM), $L_c = 40 \text{ nm}$, $f_e = 4$, and $z_0 = 5 \text{ nm}$ (fixed, from previous information on the feedback system). The graphics show that the theory agrees well with the experimental results.

It is important to notice that the value of L_c extracted from the experiment presented in Fig. 4 (40 nm) is considerably (33%) larger than measured before ($\approx 30 \text{ nm}$ in Ref. [26]). Apart from the higher quality of the experimental data presented here (larger field enhancement; more data points), this difference confirms the relevance of the TS on the calculation of the TERS intensity.

V. LIMITATIONS OF THE MODEL

The analysis presented here considers two premises: (i) the sample does not support plasmon modes for excitation fields in the visible range; (ii) the sample is sitting on a dielectric substrate. Both aspects apply to a wide class of 2D materials (including graphene, hBN, and MOS_2) deposited on SiO_2 substrates, broadly used in atomic force microscopy TERS measured under ambient conditions. However, if the sample is sitting on a metallic substrate, as it should be the case in scanning tunneling microscopy TERS, the so-called gap mode [35–39] takes place and additional considerations must be taken into account, as addressed experimentally and by numerical simulations in Ref. [30]. First, the strong coupling of the radiation field with the metallic substrate affects both

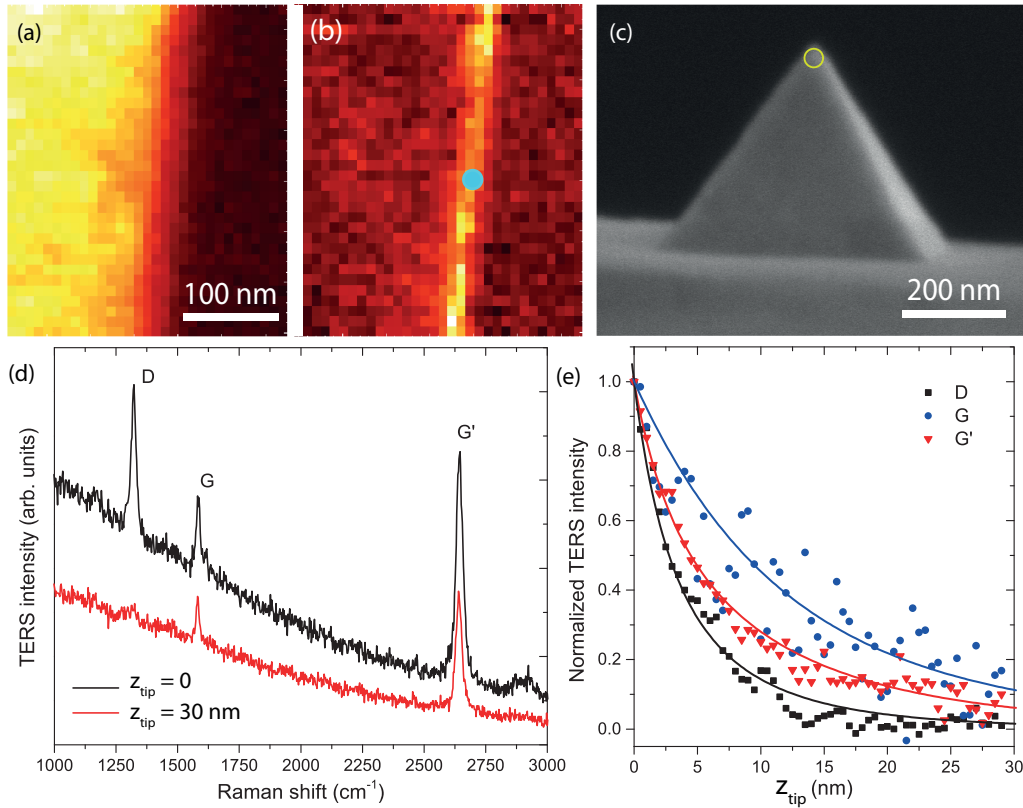


FIG. 4. TERS experiment in graphene. (a), (b) Hyperspectral TERS maps of a graphene edge, where the color scale renders the G' and D intensities, respectively. Each spectrum was recorded with 0.6 s of integration time and $120 \mu\text{W}$ of laser power, as measured at the backaperture of the objective lens. While the G' band spreads over the graphene area, the D band is confined at the edge, which therefore behaves as a one-dimensional scatterer [34]. (c) SEM image of the plasmon-tunable pyramid tip (PTTP) used in the experiment. The yellow circle indicates $r_{\text{tip}} \approx 15 \text{ nm}$. (d) TERS spectra recorded at the edge of the graphene flake, at the position indicated by the light-blue circle in panel (b), with the tip positioned at $z_{\text{tip}} = 0$ (black spectrum) and $z_{\text{tip}} = 30 \text{ nm}$ (red spectrum). (e) Normalized TERS intensities as a function of z_{tip} . Blue bullets, red down triangles, and black squares are experimental data for the G , G' , and D bands, respectively. The solid lines (blue for G , red for G' , and black for D) are the theoretical curves that fit better to the experimental data, with the parameters $r_{\text{tip}} = 15 \text{ nm}$ (fixed, as revealed by SEM), $L_c = 40 \text{ nm}$, $f_e = 4$, and $z_0 = 5 \text{ nm}$ (fixed, as previously known for the feedback system).

far-field and near-field distributions. In the far field, the in-plane polarized field is slightly narrower and the out-of-plane polarized field is moderately enhanced. In the near field, the out-of-plane components of the field are drastically changed, becoming 70% more intense and 26% narrower. For the in plane, an overall slight sharpening of field distribution is observed.

Because the presence of a metallic substrate changes some characteristics of the radiation field that characterizes the Raman interaction between sample and tip, the point dipole model [Fig. 2, Eq. (1) and related discussion] may not be a suitable description for the source of the overall excitation field in gap mode TERS. However, it does not invalidate the analysis presented here, especially considering that the changes are almost irrelevant for the in-plane component of the field, as shown in Ref. [30], which is the one responsible for the excitation of most vibrational modes in 2D systems. Nevertheless, a particularly important aspect related to symmetry should be considered in the analysis of gap mode TERS. The presence of the metallic substrate adds an extra symmetry element in the TERS process, which is a horizontal mirror at the sample plane. The symmetry of the system is then raised from $C_{\infty v}$ in the nongap mode to $D_{\infty h}$ in the gap mode and,

consequently, the TS scattering sequence becomes forbidden for both the G and $2D$ bands in gap mode [27,30].

VI. FINAL CONSIDERATIONS AND PERSPECTIVES

The importance of tip-enhanced Raman spectroscopy as an analytical tool for nanoscience and nanotechnology has grown fast over the past decades [40,41], becoming a practical instrument of research capable of delivering unprecedented scientific findings such as the direct optical observation of vibrational modes in single molecules [36,38] and the Moiré pattern in twisted bilayer graphene [42]. Parallel to the experimental advances, the theory of TERS has been modeled throughout the years, revealing a breakthrough in the fundamental interpretation of Raman scattering: due to the close proximity of the tip with the sample's surface (near-field regime), interference effects play an important role on the TERS intensity. As a consequence, the coherence length of optical phonons can be extracted from TERS data, considering the dependence of the TERS intensity with the tip-sample separation distance. These theoretical findings were reported in a series of Physical Review papers published over the past decade [19,20,24–27,30].

The current work fills in a gap of information in the literature, which is the calculation of the TERS intensity derived from the *sample-tip* (TS) sequence. As for the TST term, due to the symmetry of the Raman tensors, and consequently to the polarization of the Raman-scattered field, the interference is constructive for fields generated by totally symmetric vibrational modes and destructive otherwise. We have used graphene as a prototype for testing the theory. The results confirm that (i) due to its 1D character, the *D* band enhances considerably more than the *G* and *G'* bands and (ii) because the *G* band (E_{2g} symmetry) undergoes destructive interference and the *G'* band (A_1 symmetry) undergoes constructive interference in the TS and TST processes, the *G* band enhances less than the *G'*. These finds are summarized in Fig. 4. With the more complete picture, the value obtained for the phonon coherence length in graphene is revised to ≈ 40 nm. New

advances and refinement of the theory may be reached by considering the following aspects/subjects: (i) intermediate-field and far-field terms of the dyadic Green's function; (ii) out-of-plane modes in 2D systems; (iii) zero-dimensional (pointlike) samples; (iv) interference effects in nonlinear regimes; (v) effects of tip-substrate interaction in gap mode TERS.

ACKNOWLEDGMENTS

This work was supported by CNPq (Grants No. 302775/2018-8, No. 429771/2018-5, No. 306348/2019-5, and No. 309537/2019-3), Finep (Grant No. 442521/2019-7), CAPES (RELAII and Grant No. 36788881.198744/2018-01), and FAPEMIG Foundation (Grants No. TEC-RED-00282-16, No. APQ-02026-17, and No. CEX-APQ-01361-14).

-
- [1] R. M. Stöckle, Y. D. Suh, V. Deckert, and R. Zenobi, Nanoscale chemical analysis by tip-enhanced Raman spectroscopy, *Chem. Phys. Lett.* **318**, 131 (2000).
- [2] N. Hayazawa, Y. Inouye, Z. Sekkat, and S. Kawata, Metallized tip amplification of near-field Raman scattering, *Opt. Commun.* **183**, 333 (2000).
- [3] L. G. Cançado, A. Hartschuh, and L. Novotny, Tip-enhanced Raman spectroscopy of carbon nanotubes, *J. Raman Spectrosc.* **40**, 1420 (2009).
- [4] B.-S. Yeo, J. Stadler, T. Schmid, R. Zenobi, and W. Zhang, Tip-enhanced Raman Spectroscopy - Its status, challenges and future directions, *Chem. Phys. Lett.* **472**, 1 (2009).
- [5] J. Stadler, T. Schmid, and R. Zenobi, Developments in and practical guidelines for tip-enhanced Raman spectroscopy, *Nanoscale* **4**, 1856 (2012).
- [6] L. Langelüddecke, P. Singh, and V. Deckert, Exploring the nanoscale: fifteen years of tip-enhanced Raman spectroscopy, *Appl. Spectrosc.* **69**, 1357 (2015).
- [7] T. Deckert-Gaudig, A. Taguchi, S. Kawata, and V. Deckert, Tip-enhanced Raman spectroscopy - from early developments to recent advances, *Chem. Soc. Rev.* **46**, 4077 (2017).
- [8] F. Shao and R. Zenobi, Tip-enhanced Raman spectroscopy: Principles, practice, and applications to nanospectroscopic imaging of 2D materials, *Anal. Bioanal. Chem.* **411**, 37 (2019).
- [9] L. Novotny and B. Hecht, *Principles of Nano-Optics* (Cambridge University Press, New York, 2012).
- [10] L. Novotny and N. Van Hulst, Antennas for light, *Nat. Photon.* **5**, 83 (2011).
- [11] N. Mauser and A. Hartschuh, Tip-enhanced near-field optical microscopy, *Chem. Soc. Rev.* **43**, 1248 (2014).
- [12] C. Rabelo, H. Miranda, T. L. Vasconcelos, L. G. Cançado, and A. Jorio, Tip-enhanced Raman spectroscopy of graphene, in *2019 4th International Symposium on Instrumentation Systems, Circuits and Transducers (INSCIT)* (IEEE, São Paulo, 2019), pp. 1–6.
- [13] X. Shi, N. Coca-López, J. Janik, and A. Hartschuh, Advances in tip-enhanced near-field Raman microscopy using nanoantennas, *Chem. Rev.* **117**, 4945 (2017).
- [14] T. L. Vasconcelos, B. S. Archanjo, B. Fragneaud, B. S. Oliveira, J. Riikonen, C. Li, D. S. Ribeiro, C. Rabelo, W. N. Rodrigues, A. Jorio, C. A. Achete, and L. G. Cançado, Tuning localized surface plasmon resonance in scanning near-field optical microscopy probes, *ACS Nano* **9**, 6297 (2015).
- [15] T. L. Vasconcelos, B. S. Archanjo, B. S. Oliveira, W. F. Silva, R. S. Alencar, C. Rabelo, C. A. Achete, A. Jorio, and L. G. Cançado, Optical nanoantennas for tip-enhanced Raman spectroscopy, *IEEE J. Sel. Top. Quantum Electron.* **27**, 4600411 (2020).
- [16] T. L. Vasconcelos, B. S. Archanjo, B. S. Oliveira, R. Valaski, R. C. Cordeiro, H. G. Medeiros, C. Rabelo, A. Ribeiro, P. Ercius, C. A. Achete, A. Jorio, and L. G. Cançado, Plasmon-tunable tip pyramids: Monopole nanoantennas for near-field scanning optical microscopy, *Adv. Opt. Mater.* **6**, 1800528 (2018).
- [17] B. S. Oliveira, B. S. Archanjo, R. Valaski, C. A. Achete, L. Gustavo Cançado, A. Jorio, and T. L. Vasconcelos, Nanofabrication of plasmon-tunable nanoantennas for tip-enhanced Raman spectroscopy, *J. Chem. Phys.* **153**, 114201 (2020).
- [18] J. Sun, J. C. Schotland, and P. S. Carney, Strong probe effects in near-field optics, *J. Appl. Phys.* **102**, 103103 (2007).
- [19] L. G. Cançado, R. Beams, A. Jorio, and L. Novotny, Theory of Spatial Coherence in Near-Field Raman Scattering, *Phys. Rev. X* **4**, 031054 (2014).
- [20] C. Rabelo, T. L. Vasconcelos, B. C. Publio, H. Miranda, L. G. Cançado, and A. Jorio, Linkage Between Micro- and Nano-Raman Spectroscopy of Defects in Graphene, *Phys. Rev. Appl.* **14**, 024056 (2020).
- [21] A. R. Neto, C. Rabelo, L. G. Cançado, M. Engel, M. Steiner, and A. Jorio, Protocol and reference material for measuring the nanoantenna enhancement factor in tip-enhanced Raman spectroscopy, in *4th International Symposium on Instrumentation Systems, Circuits and Transducers (INSCIT)* (IEEE, São Paulo, 2019), pp. 1–6.
- [22] R. Carminati and J.-J. Greffet, Near-Field Effects in Spatial Coherence of Thermal Sources, *Phys. Rev. Lett.* **82**, 1660 (1999).
- [23] W. H. Carter and E. Wolf, Coherence properties of Lambertian and non-Lambertian sources, *J. Opt. Soc. Am.* **65**, 1067 (1975).

- [24] L. G. Cançado, A. Jorio, A. Ismach, E. Joselevich, A. Hartschuh, and L. Novotny, Mechanism of Near-Field Raman Enhancement in One-Dimensional Systems, *Phys. Rev. Lett.* **103**, 186101 (2009).
- [25] R. V. Maximiano, R. Beams, L. Novotny, A. Jorio and L. G. Cançado, Mechanism of near-field Raman enhancement in two-dimensional systems, *Phys. Rev. B* **85**, 235434 (2012).
- [26] R. Beams, L. G. Cançado, S.-H. Oh, A. Jorio, and L. Novotny, Spatial Coherence in Near-Field Raman Scattering, *Phys. Rev. Lett.* **113**, 186101 (2014).
- [27] A. Jorio, N. S. Mueller, and S. Reich, Symmetry-derived selection rules for plasmon-enhanced Raman scattering, *Phys. Rev. B* **95**, 155409 (2017).
- [28] R. Beams, Tip-enhanced Raman scattering of graphene, *J. Raman Spectrosc.* **49**, 157 (2018).
- [29] R. S. Alencar, C. Rabelo, H. L. S. Miranda, T. L. Vasconcelos, B. S. Oliveira, A. Ribeiro, B. C. Públio, J. Ribeiro-Soares, A. G. S. Filho, L. G. Cançado, and A. Jorio, Probing spatial phonon correlation length in post-transition metal monochalcogenide GaS using tip-enhanced Raman spectroscopy, *Nano Lett.* **19**, 7357 (2019).
- [30] H. Miranda, C. Rabelo, L. G. Cançado, T. L. Vasconcelos, B. S. Oliveira, F. Schulz, H. Lange, S. Reich, P. Kusch, and A. Jorio, Impact of substrate on tip-enhanced Raman spectroscopy: A comparison between field-distribution simulations and graphene measurements, *Phys. Rev. Research* **2**, 023408 (2020).
- [31] H. Miranda, C. Rabelo, T. L. Vasconcelos, L. G. Cançado, and A. Jorio, Optical properties of plasmon-tunable tip pyramids for tip-enhanced Raman spectroscopy, *Phys. Status Solidi* **14**, 2000212 (2020).
- [32] A. Jorio, M. S. Dresselhaus, R. Saito, and G. Dresselhaus, *Raman Spectroscopy in Graphene Related Systems* (Wiley-VCH, Weinheim, 2011).
- [33] R. Loudon, The Raman effect in crystals, *Adv. Phys.* **13**, 423 (1964).
- [34] R. Beams, L. G. Cançado, and L. Novotny, Low-temperature Raman study of the electron coherence length near graphene edges, *Nano Lett.* **11**, 1177 (2011).
- [35] W. Zhang, B. S. Yeo, T. Schmid, and R. Zenobi, Single molecule tip-enhanced Raman spectroscopy with silver tips, *J. Phys. Chem. C* **111**, 1733 (2007).
- [36] R. Zhang, Y. Zhang, Z. C. Dong, S. Jiang, C. Zhang, L. G. Chen, L. Zhang, Y. Liao, J. Aizpurua, Y. Luo, J. L. Yang, and J. G. Hou, Chemical mapping of a single molecule by plasmon-enhanced Raman scattering, *Nature (London)* **498**, 82 (2013).
- [37] S. F. Becker, M. Esmann, K. W. Yoo, P. Gross, R. Vogelgesang, N. K. Park, and C. Lienau, Gap-plasmon-enhanced nanofocusing near-field microscopy, *ACS Photon.* **3**, 223 (2016).
- [38] J. Lee, K. T. Crampton, N. Tallarida, and V. A. Apkarian, Visualizing vibrational normal modes of a single molecule with atomically confined light, *Nature (London)* **568**, 78 (2019).
- [39] J. J. Baumberg, J. Aizpurua, M. H. Mikkelsen, and D. R. Smith, Extreme nanophotonics from ultrathin metallic gaps, *Nat. Mater.* **18**, 668 (2019).
- [40] M. D. Costa, L. G. Cançado, and A. Jorio, Event chronology analysis of the historical development of tip-enhanced Raman spectroscopy, *J. Raman Spectrosc.* **52**, 587 (2021).
- [41] Z. Zhang, S. Sheng, R. Wang, and M. Sun, Tip-enhanced Raman spectroscopy, *Anal. Chem.* **88**, 9328 (2016).
- [42] A. C. Gadelha, D. A. A. Ohlberg, C. Rabelo, E. G. S. Neto, T. L. Vasconcelos, J. L. Campos, J. S. Lemos, V. Ornelas, D. Miranda, R. Nadas, F. C. Santana, K. Watanabe, T. Taniguchi, B. van Troeye, M. Lamparski, V. Meunier, V.-H. Nguyen, D. Paszko, J.-C. Charlier, L. C. Campos *et al.*, Localization of lattice dynamics in low-angle twisted bilayer graphene, *Nature (London)* **590**, 405 (2021).